Published in final edited form as:
*Phys Med Biol*. 2015 January 21; 60(2): 769–784. doi:10.1088/0031-9155/60/2/769.

# A Highly Sensitive X-ray Imaging Modality for Hepatocellular Carcinoma Detection *in Vitro*

**Danielle Rand**[1], **Edward G. Walsh, Ph.D.**[2], **Zoltan Derdak, M.D**[3], **Jack R. Wands, M.D.**[3], and **Christoph Rose-Petruck, Ph.D.**[1,*]

[1]Department of Chemistry, Brown University. 324 Brook Street, Providence, Rhode Island 02912 (USA)

[2]Department of Neuroscience, Brown University. 185 Meeting Street, Providence, Rhode Island 02912 (USA)

[3]The Liver Research Center, Rhode Island Hospital and Warren Alpert Medical School of Brown University. 55 Claverick Street, Providence, Rhode Island 02903 (USA)

## Abstract

Innovations that improve sensitivity and reduce cost are of paramount importance in diagnostic imaging. The novel x-ray imaging modality called Spatial Frequency Heterodyne Imaging (SFHI) is based on a linear arrangement of x-ray source, tissue, and x-ray detector, much like that of a conventional x-ray imaging apparatus. However, SFHI rests on a complete paradigm reversal compared to conventional x-ray absorption-based radiology: while scattered x-rays are carefully rejected in absorption-based x-ray radiology to enhance the image contrast, SFHI forms images exclusively from x-rays scattered by the tissue. In this study we use numerical processing to produce x-ray scatter images of Hepatocellular Carcinoma (HCC) labeled with a nanoparticle contrast agent. We subsequently compare the sensitivity of SFHI in this application to that of both conventional x-ray imaging and Magnetic Resonance Imaging (MRI). Although SFHI is still in the early stages of its development, our results show that the sensitivity of SFHI is an order of magnitude greater than that of absorption-based x-ray imaging and approximately equal to that of MRI. As x-ray imaging modalities typically have lower installation and service costs compared to MRI, SFHI could become a cost effective alternative to MRI, particularly in areas of the world with inadequate availability of MRI facilities.

### Keywords

X-ray Scatter Imaging; Magnetic Resonance Imaging; cancer detection; image processing; nanoparticle contrast agents

Corresponding author: Christoph Rose-Petruck, CRosePet@Brown.edu, Department of Chemistry, Brown University, 324 Brook Street, Box H, Providence, RI 02912, Phone: +1 401 863 1533, Phone 2: +1 401 863 3207, Fax: 401-863-2594.

## Introduction

In recent years, a variety of imaging techniques have been developed and investigated for their ability to utilize nanoparticle contrast agents. Some of the combinations of materials and modalities previously studied include superparamagnetic iron oxide nanoparticles (SPIONs) for Magnetic Resonance Imaging (Na et al., 2009, Stephen et al., 2011, Lee and Hyeon, 2012), gold nanoparticles (AuNPs) for x-ray Computed Tomography (CT) (Hainfeld et al., 2006, Kim et al., 2007, Popovtzer et al., 2008), and quantum dots for optical imaging (Bentolila et al., 2004, Aswathy et al., 2010). In many cases, these nano-enhanced techniques are applied in biomedical imaging for the detection and diagnosis of diseases such as cancer (Rosen et al., 2012, Vollrath et al., 2013, Kim and Jon, 2012, Mukerjee et al., 2012).

To improve cancer treatment and prognosis, innovations in diagnostic imaging that increase sensitivity and reduce cost are a necessity. To this end we report on the development of a novel x-ray imaging technique called Spatial Frequency Heterodyne Imaging (SFHI) that utilizes nanoparticle contrast agents (Rand et al., 2011, Liu et al., 2011a, Wu et al., 2012). SFHI forms an image using x-rays scattered by a sample via numerical processing, which extracts the desired information that characterizes the imaged object (Liu et al., 2011a), and the technique can be used for both biomedical and materials imaging applications (Rand et al., 2011, Liu et al., 2011a, Wu et al., 2012, Wen et al., 2008, Wen et al., 2009, Stein et al., 2010). Previous results have shown that SFHI can be used to distinguish AuNP-labeled liver cancer tissue from tissue that is unlabeled, and these studies indicate that SFHI is more sensitive to the contrast provided by nanoparticle probes than traditional absorption-based x-ray imaging.(Rand et al., 2011) In the current report, we show that SFHI can also detect the labeling of liver cancer tissue with SPIONs. Furthermore, comparisons with available clinical imaging techniques suggest that the sensitivity of SFHI in this application approaches that of MRI and surpasses that of absorption-based x-ray imaging.

SFHI is similar to other scattering-based x-ray imaging techniques found in the literature that utilize incoherent x-ray sources. Wen et al. have used the technique to distinguish materials that have identical x-ray absorption properties and to reveal bone structure and density information in rats and pigs (Wen et al., 2008, Wen et al., 2009). Similarly, Pfeiffer and coworkers have shown that conventional x-ray tube sources and absorption gratings such as those described in this study can yield images based on small-angle x-ray scattering that are different from and often complementary to absorption-based x-ray images (Pfieffer et al., 2008). Others have applied similar types of scattering-based x-ray techniques in the biomedical arena, for example investigating the x-ray scattering properties of breast cancer tissue (Stampanoni et al., 2011, Endrizzi et al., 2014). However, much of the previous work has focused on x-ray scattering by micron-sized structures (Yashiro et al., 2010). We believe our group has demonstrated the first successful attempt at using sub-100 nm nanoparticles as contrast agents in scattering-based x-ray imaging. Metal nanoparticles such as those used here are very promising as x-ray scatter contrast agents due to their high electron density and large surface area, their small size suitable for intravenous injection, and the ease with which their surfaces can be modified for targeted delivery *in vivo*.

The type of liver cancer studied here, Hepatocellular Carcinoma (HCC), is the most common form of liver cancer in adults (El-Sarag and Mason, 1999). According to the most recent estimates by the American Cancer Society, over 700,000 people are diagnosed with this disease each year worldwide, and over 600,000 of these cases result in death. Interestingly, the incidence of HCC is highest in sub-Saharan Africa and Southeastern Asia (Trevisani et al., 2008, O'Brien et al., 2004). SFHI consequently has a distinct advantage over MRI for use in the diagnostic imaging of HCC in these areas of the world, as x-ray imaging modalities are typically less expensive and more widely available than MRI (Huang et al., 2012, Sistrom and McKay, 2005, Griebsch et al., 2006). Because the arrangement of source, patient, and detector in SFHI is identical to that used for conventional x-ray imaging, upgrading existing x-ray machines for SFHI service will be possible. With further development, SFHI could therefore become a viable, low cost supplement or alternative to techniques like MRI for biomedical imaging applications. Additionally, our discovery that SPIONs can provide appreciable contrast in SFHI has implications for dual-modality imaging: with the use of a single SPION probe, MRI and SFHI could be combined to offer a technique with a synergistic advantage over either modality alone.

## Materials and Methods

Gold nanoparticles (10 nm diameter) stabilized by citrate buffer were purchased from British Biocell International (Cardiff, UK). Water-soluble iron oxide nanoparticles (10 nm diameter) coated with poly(ethylene glycol) (PEG) were purchased from Ocean NanoTech (Springdale, AR). Additionally, water-soluble iron oxide nanoparticles (10 nm and 40 nm diameter) with an amphiphilic polymer coating containing carboxylic acid reactive groups were purchased from Ocean NanoTech. We will refer to the above as-purchased nanoparticles as AuNP-cit, SPION-PEG, and SPION-COOH, respectively. All other chemicals were purchased from Sigma Aldrich (St. Louis, MO).

### PEG coating of gold nanoparticles

For SFHI of gold nanoparticles suspended in water, the as-purchased AuNP-cit were stabilized with a coating of functionalized polyethylene-glycol (PEG). HS-PEG-COOH ($M_w$ = 3000) was prepared at 100 μM in nanopure water. To 50 μg of AuNP-cit nanoparticles (10 nm diameter) in water, 140 μL of PEG was added and stirred overnight at room temperature. The chains of functionalized PEG attach to the surface of the gold nanoparticles during this mixing, replacing the citrate stabilizer due to the affinity of thiols for gold (Jokerst et al., 2011, Brandenberger et al., 2010). Excess PEG was removed by centrifugation, and the resulting AuNP-PEG nanoparticles were resuspended in nanopure water.

### Polyelectrolyte coating of superparamagnetic iron oxide nanoparticles

To enhance the uptake of iron oxide nanoparticles by living cells, 10 nm and 40 nm SPIONs were coated with the cationic polyelectrolyte poly(allylamine hydrochloride) (PAH). A stock solution of PAH was prepared at 10 mg/mL in 1mM aqueous NaCl. Suspensions of SPION-COOH nanoparticles were prepared in nanopure water at 50 μg Fe/mL. To 50 μg of SPION-COOH, 50 μL PAH (for 10 nm nanoparticles) or 200 μL PAH (for 40 nm nanoparticles) was added and mixed vigorously. After 30 min adsorption time, excess

polymer in the supernatant was removed by centrifugation, and the resulting SPION-COOH-PAH nanoparticles were resuspended in nanopure water.

### Cell culture

A human hepatocellular carcinoma cell line (FOCUS) was obtained from the Wands Lab (Brown University/Rhode Island Hospital, Providence, RI).(He et al., 1984) Cells were maintained in Eagle's Minimum Essential Medium (EMEM) supplemented with 10% fetal bovine serum, 1% penicillin/streptomycin and 1% L-glutamine. Cells were grown at 37°C in an atmosphere of 5% $CO_2$.

### Cellular uptake of polyelectrolyte-coated iron oxide nanoparticles

FOCUS cells were grown to near confluency in T75 tissue culture flasks. Prior to incubation with SPIONs, the medium was removed, and cells were washed with serum-free EMEM. SPION-COOH-PAH nanoparticle suspensions containing either 50 μg or 100 μg of iron were added to the flasks along with 5 mL serum-free EMEM, resulting in incubation solutions that were 10 and 20 ppm in iron, respectively. Cells were incubated with the SPIONs for 5h at 37°C in an atmosphere of 5% $CO_2$. After incubation, the cell culture medium and remaining free nanoparticles were removed, and cells were detached from flasks using trypsin-EDTA. Trypsinized cells were collected by centrifugation and washed with PBS. Cells were fixed using 4% formaldehyde and washed again with PBS.

### Preparation of iron oxide samples in gel for imaging

Agarose gel was prepared at 2.5% by weight by dissolving 250 mg agar in 10 mL PBS at 80 °C for 20 min. 160 μL of gel was mixed with 840 μL of the sample to be imaged (either SPION-PEG nanoparticles suspended in water, or cells containing SPION-COOH-PAH nanoparticles suspended in PBS), giving samples of approximately 1 mL total volume. Samples were allowed to set for 24h before imaging.

### Spatial Frequency Heterodyne Imaging (SFHI)

The x-ray imaging technique applied here, called Spatial Frequency Heterodyne Imaging, (Wen et al., 2008, Wen et al., 2009, Stein et al., 2010, Rand et al., 2011, Liu et al., 2011a, Wu et al., 2012) uses x-rays scattered by the sample to form an image. The sample's deflection of incident x-rays from the primary beam direction is detected by placing a grid between the sample and the x-ray detector (see Figure 1).Without sample, the image of the grid shows intensity modulations limited only by the resolution of the imaging system. X-rays scattered by the sample cause a blurring of the grid image. The extent of this blurring corresponds to the amount of x-rays that are scattered by the sample, and is therefore a measure of nanoparticle concentration. The imaging theory is discussed elsewhere.(Wu et al., 2012)

Acquired images can be analyzed by a procedure involving Fourier transformation. The image intensity modulations are proportional to the product of the x-ray transmittances of the sample and of the grid. Thus, Fourier transformation of the image converts this product into a convolution in the spatial frequency domain (see Figure 2). The grid, a periodic structure, produces a series of peaks in this convolution, and each peak is surrounded by the

spatial frequency spectrum of the sample. The areas surrounding all peaks therefore contain the same information regarding x-ray transmittance through the sample. X-ray scatter does not influence the intensities around the central, zero-frequency peak, but does influences the intensities around all other higher order peaks. Selecting an area around the zero-order peak and an area around at least one other higher order peak and Fourier back-transforming these areas results in two separate images. The image $h_0$ from the zero-order area contains only x-ray transmittance information. The image $h_x$ from the higher order area contains both x-ray transmittance and x-ray scatter information. For normalization purposes, an image is acquired without sample and processed following the same Fourier procedure, resulting in one zero-order image $g_0$ and one higher-order image $g_x$ of the grid. Subsequently, a normalized absorbance image and one or more normalized scatter images are produced according to Equation 1 and Equation 2.

$$A = -\log_{10}\left(\frac{h_0}{g_0}\right) \quad (1)$$

$$S = -\log\left(\frac{h_x/g_x}{h_0/g_0}\right) \quad (2)$$

Thus, $S$ consists exclusively of scattered x-rays because the transmittance component is normalized out. By convention, the absorbance $A$ is defined as the logarithm of the ratio of the transmittances $h_0$ and $h_x$. The scattered intensity $S$ is the logarithm of the amount of scattered radiation. Use of the logarithm in Equations 1 and 2 yields values that are linearly related to sample thickness.

The image processing concept is schematically depicted in Figure 2. The zero-order peak (blue box) in the convolution yields the absorbance image $A$. The 1st order peaks (red and yellow boxes) in the convolution yield the scatter images $S$. Note that the left 1st order peak (red box) contains radiation scattered only in the horizontal direction; by convention we label this image the “1,0” scatter image after processing. Similarly, the upper 1st order peak (yellow box) corresponds to scattering in the vertical direction, and gives a “0,1” scatter image after processing. Thus, every x-ray image taken yields three types of processed images; one corresponding to x-radiation absorbed by the sample, one corresponding to x-radiation scattered horizontally by the sample, and one corresponding to x-radiation scattered vertically by the sample. It should be noted that although this technique is capable of giving anisotropic scattering information, both 1st order x-ray images should measure identical scatter signals when isotropically-oriented nanoparticles are used as SFHI contrast agents.

X-ray measurements were done with a microfocus X-ray tube (Trufocus Corp., model TFX-3110EW) with a tungsten anode. The tube was operated at an electrical power of 16W, with an anode voltage of 80 kV. Such a high voltage is used to reduce required exposure times; it is also better suited for applications requiring large penetration depths. The distance between the source and sample is 0.4 m, and the distance between the sample and detector is 1.2 m. The grid used is a nickel wire mesh with a pitch of approximately 170 μm. The grid

was approximately 5 cm long and 5 cm wide with a wire thickness of 66 μm; it was purchased from Small Parts, Inc. (Seattle, WA), and was positioned between the x-ray source and the sample, directly in front of the sample. The images were acquired with an X-ray CMOS detector (Rad-Icon Imaging, RadEye200 model) with a pixel size of 98 μm. The total exposure time for each image was 180 s. Mean signal enhancements relative to a control sample were taken from regions measured in three separate x-ray images Errors were calculated by taking the standard deviation of the mean from these regions over all three images. The regions chosen in each image for analysis included the central 80% of the vial to avoid x-ray absorbance or scatter by the vial edges. All samples for x-ray and MR imaging were prepared in Eppendorf tubes with a diameter and thickness of approximately 1 cm.

X-ray absorbance signal enhancements due to the presence of nanoparticles in each sample were calculated by normalizing the absorbance signal A for each sample by that of a control sample containing no nanoparticles (see Equation 3). Similarly, the x-ray scatter signal enhancements due to the presence of nanoparticles in each sample were calculated by normalizing the x-ray scatter signal S of the sample by that of a control containing no nanoparticles (see Equation 4).

$$A_{enhancement} = \frac{A_{sample}}{A_{control}} \quad (3)$$

$$S_{enhancement} = \frac{S_{sample}}{S_{control}} \quad (4)$$

## Magnetic Resonance Imaging (MRI)

MRI data were acquired using a Siemens Tim Trio scanner with main field strength of 3 Tesla. The body volume resonator was used for transmission while a 32 element volume array was used for signal receive. Vials were arranged horizontally within the receiver array. Samples were at room temperature at the time of scanning. Following acquisitions of scout images for tomographic plane selection, spin echo image data sets were obtained with a repetition time of 3000 ms, echo times of 10–180 ms in 10 ms steps, and a slice thickness of 3 mm. In-plane resolution was 0.56 mm. $T_2$ maps were computed by use of a three parameter (equilibrium magnetization, $T_2$ and offset) nonlinear least squares curve fit of signal intensity vs echo time for the spin echo signal equation on a pixel basis using Matlab scripts (MathWorks, Natick, MA). Mean $T_2$ values (and standard deviations) were taken from the region representing the center 80% of the imaged vial cross-sections. There were approximately 100 pixels in each region of interest.

## Determination of iron content in cell pellets

The amount of iron taken up by FOCUS cells during incubation was determined by inductively-coupled plasma atomic emission spectroscopy (ICP-AES). Samples were prepared for ICP-AES analysis by digesting iron and organics with aqua regia followed by dilution in 2% nitric acid.

## Results

### Comparison of AuNPs and SPIONs as X-ray Contrast Agents

X-ray absorbance images and SFHI x-ray scatter images were taken of gold and iron oxide nanoparticles of comparable sizes. 10 nm SPIONs coated with polyethylene glycol (type: SPION-PEG) were prepared in nanopure water at concentrations ranging from 250–1000 ppm iron concentration. 10 nm citrate-stabilized AuNPs (type: AuNP-cit) were coated with PEG via ligand exchange of PEG for citrate. The resulting suspensions of AuNP-PEG were then prepared in nanopure water at concentrations ranging from 250–1000 ppm gold concentration.

X-ray images were taken of these AuNP-PEG and SPION-PEG suspensions and analyzed. Analysis involved measuring the signals detected for the nanoparticle samples and normalizing them relative to the signal detected for a control containing only nanopure water. The subsequent signal enhancements over water for both the x-ray absorbance images and the SFHI x-ray scatter images are given as percentages in Table 1. X-ray scatter signal enhancements over water for the AuNP-PEG and SPION-PEG suspensions overlap over the range of metal concentrations studied, with signal enhancements ranging from 4.6% to 12.0% for AuNP-PEG and 6.1% to 9.7% for SPION-PEG. X-ray scatter signal enhancements are also larger than x-ray absorbance signal enhancements by approximately a factor of 10.

### Comparison of SFHI and MRI Using SPION Samples

SFHI x-ray scatter images and MR images were taken of iron oxide nanoparticles of varying sizes. 10 nm and 40 nm SPION-PEG were prepared in agarose gel at concentrations ranging from 0–100 ppm iron concentration. $T_2$ relaxation times were measured from the acquired MR images and are given in Table 2. Calculated relaxivities for the 10 nm SPION-PEG and 40 nm SPION-PEG are 58.21 $s^{-1}mM^{-1}$ and 21.21 $s^{-1}mM^{-1}$ respectively. After MR imaging, the 10 and 40 nm SPION-PEG samples were also imaged by SFHI. In the image analysis, x-ray scatter signals detected for the nanoparticle samples were normalized relative to the signal detected for a control containing the gel alone. The normalized x-ray scatter signal enhancements are given as percentages in Table 2. The larger 40 nm SPIONs scatter x-rays slightly more than the 10 nm SPIONs.

### Comparison of SFHI, MRI and X-ray Absorbance Imaging Using SPION+HCC samples

X-ray absorbance images, SFHI x-ray scatter images, and MR images were taken of samples containing HCC cells labeled with iron oxide nanoparticles. The cell line used is a human hepatocellular carcinoma line called the FOCUS cell line (He et al., 1984). For these studies *in vitro*, 10 nm and 40 nm SPIONs with an amphiphilic polymer coating containing carboxylic acid reactive groups (type: SPION-COOH) were coated with a layer of poly(acrylic acid) (PAH) to make them more biocompatible. The addition of PAH to the nanoparticle surface to form SPION-COOH-PAH increases the zeta potential of the nanoparticles and their cellular uptake *in vitro* (see Table 3).

For preparation of the biological samples to be used for imaging, 10 nm and 40 nm SPION-COOH-PAH were incubated with $3 \times 10^6$ HCC cells at either 10 ppm or 20 ppm for 5h at 37°C. After incubation, excess nanoparticles were washed away, and the cells containing nanoparticles were collected and fixed in formaldehyde. Fixed cells were then set in agarose gel for imaging. MR images were taken of these biological samples (see Figure 3) and $T_2$ relaxation times were measured (see Table 4). X-ray absorbance and SFHI x-ray scatter images were also taken of the biological samples; a sample SFHI x-ray scatter image of FOCUS cells incubated with 10 nm SPION-COOH-PAH at 20 ppm iron concentration is shown in Figure 4. Image analysis involved measuring the signals detected for samples containing SPION-labeled HCC cells and normalizing them by the signal detected for a control containing unlabeled HCC cells. The normalized signal enhancements are given as percentages in Table 4. After imaging was completed, iron content in the HCC cells was measured by inductively-coupled plasma atomic emission spectroscopy (ICP-AES) (see Table 4).

## Discussion

One major benefit of SFHI is its versatility, as the technique is not specific to any one material for contrast. The only requirement for a SFHI contrast agent to be used in biomedical imaging applications is an electron density that differs from that of the biological tissues being studied. As such, a wide variety of different types of nanoparticles could be used to provide contrast in SFHI x-ray scatter images. While we have had success in the past using AuNPs,(Rand et al., 2011) we show here that SPIONs are also suitable for use as contrast agents in SFHI. These metal nanoparticles scatter x-rays more than biological tissues due to their higher electron densities and their large surface areas. X-rays are scattered by electrons and at material interfaces where they encounter a change in index of refraction. Nanoparticles (and metal nanoparticles in particular) are therefore especially promising as x-ray scatter contrast agents.

To determine the feasibility of using SPIONs as contrast agents for SFHI, the ability of 10 nm gold and iron oxide nanoparticles to scatter x-rays was compared. Our results indicate that the contrast provided by SPIONs in SFHI is comparable to that provided by AuNPs, as scatter signal enhancements for both types of nanoparticles overlap over the same range of metal concentrations. Interestingly, although the x-ray scattering properties of the AuNP-PEG and SPION-PEG are similar, the SPION-PEG are weaker x-ray absorbers than their AuNP counterparts. Relative to their absorbing power, therefore, SPION-PEG are actually stronger x-ray scatterers than AuNP-PEG. Overall, SPIONs seem to be as effective as AuNPs at providing contrast in SFHI. We can therefore reasonably expect that results obtained in the past using AuNP contrast agents (for example, the differentiation of nanoparticle-labeled and unlabeled liver cancer tissue with SFHI) (Rand et al., 2011) should be possible with SPIONs as well.

The gold and iron oxide nanoparticles were also studied for their potential as contrast agents in absorption-based x-ray imaging. The results show that SFHI is a much more sensitive technique than conventional x-ray imaging, as x-ray scatter signal enhancements are an order of magnitude larger than their absorbance counterparts. While gold nanoparticles have

been used in the past to provide contrast in absorption-based x-ray imaging, the mass of gold required to provide appreciable contrast was often very large (Kim et al., 2007, Popovtzer et al., 2008, Hainfeld et al., 2006, Hainfeld et al., 2004). Our results suggest that the enhanced sensitivity of SFHI could make nanoparticle-enhanced x-ray imaging more feasible, as it should require a much lower dose of contrast agent.

Furthermore, because the arrangement of source, patient, and detector in SFHI is identical to that used for conventional x-ray imaging, the process to upgrade existing x-ray machines for SFHI service will be straightforward. The modifications made to conventional x-ray machines will not affect their ability to provide absorption-based images and, as such, it will be possible to deliver both x-ray absorbance and x-ray scatter images using a single x-ray apparatus. Tests of SFHI in a clinical setting are currently underway using a GE 100a XRI projection x-ray source at Massachusetts General Hospital. This equipment (typically used for chest radiography) has a spot size of 300 μm and x-ray energies of approximately 70keV. SFHI of a variety of samples was successful on this machine with exposure times of only 12.5 ms, indicating the potential for application of SFHI *in vivo* in human patients..

The ability of SPIONs to provide contrast in SFHI is an important discovery because it allows us to benchmark the novel x-ray imaging technique with the established and ubiquitous MRI. To directly compare the sensitivities of MRI and SFHI, the measured $T_2$ relaxation times given in Table 2 were converted to $r_2$ relaxation rates, where $r_2 = 1/T_2$. Figure 5 shows how the signals measured in both MRI and SFHI change with increasing iron concentration; both $r_2$ and x-ray scatter signal enhancement increase steadily as iron concentration rises. However, this change in signal relative to the change in iron concentration is much larger for MRI than for SFHI, suggesting that MRI benefits from enhanced sensitivity over SFHI. Interestingly, while the smaller 10 nm SPION-PEG appears to be a better $T_2$ contrast agent in the MR images (i.e., 10 nm SPION-PEG has a larger calculated relaxivity than 40 nm SPION-PEG), the larger 40 nm SPION-PEG provides more contrast in images taken by SFHI.

To examine the potential for using SPIONs in biomedical SFHI applications, and to see how SFHI compares to MRI and conventional x-ray imaging in a biomedical setting, we prepared biological samples containing liver cancer cells labeled with SPIONs. SPIONs of varying sizes were coated with a layer of polyelectrolyte and incubated with HCC cells. Previous studies have shown that weak polyelectrolyte coatings make surfaces more cytophylic (Mendelsohn et al., 2003) and can increase the cellular uptake of nanoparticles *in vitro* (Rand et al., 2011) and *in vivo* (Brandenberger et al., 2010). Here, we use the cationic PAH as a coating on top of the as-purchased SPION-COOH. The negative charge on the surface of the SPION-COOH coupled with the positive charge of the PAH allows for layer-by-layer adsorption of PAH onto the 10 nm and 40 nm SPIONs. The resulting positively-charged nanoparticles were taken up into the HCC cells during the 5h incubation period.

When cells are incubated with untargeted, cytophylic nanoparticles like the polyelectrolyte-coated SPIONs used here, passive uptake of the nanoparticles causes them to agglomerate inside the cell, often within vesicles a few hundred nm in diameter (Brandenberger et al., 2010, Walkey et al., 2012, Bartneck et al., 2010). The cells also clump together after

incubation with the nanoparticles, as the heavier iron-loaded cells become more compact when they are spun down during washing steps, and the cell pellets become harder to break apart. This clumping effect appears to significantly reduce the $T_2$ relaxation effect of the SPIONs. Compared to the samples containing only SPIONS in gel (Table 2), the $T_2$ relaxation times of the biological samples (Table 4) are much longer. On the contrary, aggregation of the nanoparticles within the HCC cells seems to lead to better contrast in SFHI: the maximum signal enhancement seen for these biological samples (Table 4) is almost double that seen for the samples containing SPION in gel alone (Table 2). The reduced effect of the contrast agent in MRI coupled with the enhanced effect of the contrast agent SFHI causes the sensitivities of the two techniques to converge in this application.

Table 5 shows the change in measured signal for each biological sample due to nanoparticle content (relative to that measured for HCC cells alone) as seen in x-ray absorbance imaging, SFHI, and MRI. The values for MRI were calculated from the $T_2$ relaxation times given in Table 4. To compare the three imaging modalities, the relative sensitivities of the techniques were calculated by taking the ratio of the signal enhancements shown at the left of Table 5. When the three techniques are compared using HCC cells loaded with nanoparticle contrast agents, we find that SFHI is more sensitive than traditional x-ray imaging by an average factor of 16, while MRI is more sensitive than SFHI by an average factor of 4. Sensitivities of SFHI and MRI start to converge especially when 40 nm SPIONs are used as contrast agents, as the larger nanoparticles provide higher contrast than smaller nanoparticles in SFHI, but lower contrast than smaller nanoparticles in MRI. Specifically, for imaging of HCC cells incubated with 40 nm SPIONs at 10 ppm, MRI is more sensitive than SFHI by a factor of just 1.9. As SFHI is a technique that has only been developed in recent years, we believe that a relative sensitivity within a factor of 2 of the more sophisticated MRI suggests significant promise for further improvements in SFHI performance.

Furthermore, Table 5 also shows that although MRI is more sensitive than SFHI, it also has a larger error. If we calculate at the size of the standard deviation in each measurement relative to the change in signal measured, we find that the error in MRI is almost twice as large as that in SFHI: for SFHI, the standard deviation is on average 2.7% of the total signal enhancement measured, while for MRI, the standard deviation is on average 5.0% of the total signal enhancement measured. The uncertainty in MRI relative to SFHI was calculated by taking the ratio of the sizes of the standard deviations in each technique; these relative uncertainties are shown for each sample in Table 5. Although MRI is on average four times more sensitive than SFHI, it is also on average twice as uncertain. We take this into account by calculating a final image enhancement parameter where the relative sensitivity of MRI is normalized by its relative uncertainty. When the size of the technique uncertainty is accounted for, we find that SFHI is approximately equal to MRI in terms of image quality.

## Conclusion

Images taken of SPIONS alone by SFHI and MRI show that the change in measured signal with changing iron concentration is much larger for MRI than for SFHI. However, when the nanoparticles begin to clump together inside cells (as they would in many diagnostic imaging applications), the image quality of SFHI is comparable to that of MRI. In fact, the

sensitivity of SFHI seems to be improved when used for biomedical imaging applications relative to pure materials applications. For a technique in the earliest stages of development, we believe SFHI shows significant promise. With further development, the sensitivity of SFHI could be improved to eventually match or overcome that of MRI.

Although a powerful technique, MRI suffers disadvantages in the high cost of its operation, maintenance, and materials, in its limited availability, and in the fact that its use requires highly trained personnel (Huang et al., 2012, Griebsch et al., 2006). On the other hand, x-ray techniques similar to SFHI have the benefit of being much cheaper and more widely available (Lee and Chen, 2009). Specifically, x-ray imaging applications such as mammography for examining breast cancer (Griebsch et al., 2006, Moore et al., 2009), CT for guided bone biopsies (Alanen et al., 2004), and CT for the diagnosis of hepatocellular carcinoma (Arguedas et al., 2003) have been shown to be more cost-effective than MRI. With improved sensitivity, SFHI could therefore be a viable and cost-effective alternative to MRI for many biomedical imaging applications, including the early diagnosis of HCC using nano-labels. It is feasible that SFHI could be implemented in underdeveloped areas of the world where HCC is common but MRI facilities are somewhat rare.

A valid comparison between x-ray imaging techniques and MRI must make note of the fact that MRI delivers no ionizing radiation to the patient. As such, the radiation dose delivered to the tissue being imaged is an important piece of information in a study benchmarking SFHI with MRI. The radiation dose delivered to the HCC cells imaged here is 1.05 Sv. However, this dose would be significantly reduced when shorter exposure times and clinical x-ray sources operating at a higher power are used. Furthermore, the radiation dose delivered to the tissues in SFHI is reduced relative to conventional x-ray imaging, as placement of the absorption grid between the x-ray source and sample in SFHI decreases the amount of radiation that reaches the patient.

Additionally, the discovery that SPIONs are suitable for use as contrast agents in SFHI could be an important step in the development of a potential dual-modality imaging technique combining SFHI and MRI. Multi-modal imaging has become popular in recent years, as different imaging techniques can often be complementary rather than competitive. Examples include combinations of Positron Emission Tomography and MRI (PET-MRI), PET and Computed Tomography (PET-CT), MRI and ultrasound imaging (US), and MRI and CT (Cheon and Lee, 2008, Lee and Chen, 2009, Jennings and Long, 2009, Huang et al., 2012). Combining multiple techniques is a potentially powerful strategy for improving image quality and diminishing the disadvantages that limit individual techniques. However, most nanoprobes developed for multi-modality imaging require multiple parts for increased functionality, often leading to additional synthetic steps and costs (Cheng et al., 2012). Examples include SPIONs that are coated with gold for US/MRI/electron microscopy (Jin et al., 2010), US microbubbles that are filled with SPIONs for dual US/MRI (Liu et al., 2011b), and AuNPs that are attached to Gadolinium chelates for dual CT/MRI (Alric et al., 2008). However, we have shown here that unmodified SPIONs can act as nanoprobes for both SFHI and MRI. A simple nanoprobe that is effective in multiple imaging modalities and doesn’t require many different components could be beneficial in terms of reducing cost and expediting the imaging process.

## Acknowledgements

C.R.P. acknowledges financial support for the development of the X-ray imaging modality by the U.S. Department of Energy under Grant DE-FG02-08ER15937. J.R.W. acknowledges financial support by the National Institutes of Health under Grant CA123544.

## References

Alanen J, Keski-Nisula L, Blano-Sequeiros R, Tervonen O. Cost comparison analysis of low-field (0.23 T) MRI- and CT-guided bone biopsies. European Radiology. 2004; 14:123–128. [PubMed: 12827428]

Alric C, Taleb J, Le Duc G, Mandon C, Billotey C, Le Meur-Herland A, Brochard T, Vocanson F, Janier M, Perriat P, Roux S, Tillement O. Gadolinium Chelate Coated Gold Nanoparticles as Contrast Agents for both X-ray Computed Tomography and Magnetic Resonance Imaging. J. Am. Chem. Soc. 2008; 130:5908–5915. [PubMed: 18407638]

Arguedas MR, Chen VK, Aloubeidi ME, Fallon MB. Screening for Hepatocellular Carcinoma in Patients with Hepatitis C Cirrhosis: A Cost-Utility Analysis. The American Journal of Gastroenterology. 2003; 98:679–690. [PubMed: 12650806]

Aswathy RG, Yoshida Y, Maekawa T, Kumar DS. Near-infrared quantum dots for deep tissue imaging. Analytical and Bioanalytical Chemistry. 2010; 397:1417–1435. [PubMed: 20349348]

Bartneck M, Keul HA, Singh S, Czaja K, Bornemann J, Bockstaller M, Moeller M, Zwadlo-Klarwasser G, Groll J. Rapid Uptake of Gold Nanorods by Primary Human Blood Phagocytes and Immunomodulatory Effects of Surface Chemistry. ACS Nano. 2010; 4:3073–3086. [PubMed: 20507158]

Bentolila LA, Ebenstein Y, Weiss S. Quantum Dots for In Vivo Small-Animal Imaging. The Journal of Nuclear Medicine. 2004; 50:493–496.

Brandenberger C, Muhlfeld C, Zulqurnain A, Lenz A, Schmid O, Parak WJ, Gehr P, Rothen-Rutishauser B. Quantitative Evaluation of Cellular Uptake and Trafficking of Plain and Polyethylene Glycol-Coated Gold Nanoparticles. Small. 2010; 6:1669–1678. [PubMed: 20602428]

Cheng Z, Al Zaki A, Hui JZ, Muzykantov VR, Tsourkas A. Multifunctional Nanoparticles: Cost Versus Benefit of Adding Targeting and Imaging Capabilities. Science. 2012; 338:903–910. [PubMed: 23161990]

Cheon J, Lee J. Synergistically Integrated Nanoparticles as Multimodal Probes for Nanobiotechnology. Accounts of Chemical Research. 2008; 41:1630–1640. [PubMed: 18698851]

El-Sarag HB, Mason AC. Rising Incidence of Hepatocellular Carcinoma in the United States. The New England Journal of Medicine. 1999; 340:745–750. [PubMed: 10072408]

Endrizzi M, Diemoz PC, Millard TP, Jones JL, Speller RD, Robinson IK, Olivo A. Hard X-ray dark-field imaging with incoherent sample illumination. Applied Physics Letters. 2014; 104:024106.

Griebsch I, Brown J, Boggis C, Dixon A, Dixon M, Easton D, Eeles R, Evans DG, Gilbert FJ, Thompson D, Turnbull LW, Walker LG, Warren R, Leach MO. Cost-effectiveness of screening with contrast enhanced magnetic resonance imaging vs X-ray mammography of women at a high familial risk of breast cancer. British Journal of Cancer. 2006; 95:801–810. [PubMed: 17016484]

Hainfeld JF, Slatkin DN, Focella TM, Smilowitz HM. Gold nanoparticles: a new X-ray contrast agent. The British Journal of Radiology. 2006; 79:248–253. [PubMed: 16498039]

Hainfeld JF, Slatkin DN, Smilowitz HM. The use of gold nanoparticles to enhance radiotherapy in mice. Physics in Medicine and Biology. 2004; 49:309–315.

He L, Isselbacher KJ, Wands JR, Goodman HM, Shih C, Quaroni A. Establishment and Characterization of a New Human Hepatocellular Carcinoma Cell Line. In Vitro. 1984; 20:493–504. [PubMed: 6086498]

Huang Y, He S, Cao W, Cai K, Liang X. Biomedical nanomaterials for imaging-guided cancer therapy. Nanoscale. 2012; 4:6135–6149. [PubMed: 22929990]

Jennings LE, Long NJ. 'Two is better than one' - Probes for dual-modality molecular imaging. Chem. Commun. 2009; 24:3511–3524.

Jin Y, Jia C, Huang S, O'donnell M, Gao X. Multifunctional nanoparticles as coupled contrast agents. Nature Communications. 2010; 1:1–8.

Jokerst JV, Lobovkina T, Zare RN, Gambhir SS. Nanoparticle PEGylation for imaging and therapy. Nanomedicine. 2011; 6:715–728. [PubMed: 21718180]

Kim D, Jon S. Gold nanoparticles in image-guided cancer therapy. Inorganica Chimica Acta. 2012; 393:154–164.

Kim D, Park S, Lee JH, Jeong YY, Jon S. Antibiofouling Polymer-Coated Gold Nanoparticles as a Contrast Agent for in Vivo X-ray Computed Tomography Imaging. J. Am. Chem. Soc. 2007; 129:7661–7665. [PubMed: 17530850]

Lee N, Hyeon T. Designed synthesis of uniformly sized iron oxide nanoparticles for efficient magnetic resonance imaging contrast agents. Chem. Soc. Rev. 2012; 41:2575–2589. [PubMed: 22138852]

Lee S, Chen X. Dual-Modality Probes for In Vivo Molecular Imaging. Molecular Imaging. 2009; 8:87–100. [PubMed: 19397854]

Liu Y, Ahr B, Linkin A, Diebold GJ, Rose-Petruck C. X-ray spatial harmonic imaging of phase objects. Optics Letters. 2011a; 36:2209–2211. [PubMed: 21685969]

Liu Z, Lammers T, Ehling J, Fokong S, Bornemann J, Kiessling F, Gatiens J. Iron oxide nanoparticle-containing microbubble composites as contrast agents for MR and ultrasound dual-modality imaging. Biomaterials. 2011b; 32:6155–6163. [PubMed: 21632103]

Mendelsohn JD, Yang SY, Hiller JA, Hochbaum AI, Rubner MF. Rational Design of Cytophilic and Cytophobic Polyelectrolyte Multilayer Thin Films. Biomacromolecules. 2003; 4:96–106. [PubMed: 12523853]

Moore SG, Shenoy PJ, Fanucchi L, Tumeh JW, Flowers CR. Cost-effectiveness of MRI compared to mammography cancer screening in a high risk population. BMC Health Services Research. 2009; 9:1–8. [PubMed: 19118494]

Mukerjee A, Ranjan AP, Vishwanatha JK. Combinatorial Nanoparticles for Cancer Diagnosis and Therapy. Current Medicinal Chemistry. 2012; 19:3714–3721. [PubMed: 22680922]

Na HB, Song IC, Hyeon T. Inorganic Nanoparticles for MRI Contrast Agents. Adv. Mat. 2009; 21:2133–2148.

O'brien TR, Kirk G, Zhang M. Hepatocellular Carcinoma: Paradigm of Preventative Oncology. The Cancer Journal. 2004; 10:67–73. [PubMed: 15130266]

Pfieffer F, Bech M, Bunk O, Kraft P, Eikenberry EF, Bronnimann C, Grunzweig C, David C. Hard X-ray dark-field imaging using a grating interferometer. Nature Materials. 2008; 7:134–137.

Popovtzer R, Agrawal A, Kotov NA, Popovtzer A, Balter J, Carey TE, Kopelman R. Targeted Gold Nanoparticles Enable Molecular CT Imaging of Cancer. Nano Letters. 2008; 8:4593–4596. [PubMed: 19367807]

Rand D, Ortiz V, Liu Y, Derdak Z, Wands JR, Taticek M, Rose-Petruck C. Nanomaterials for X-ray Imaging: Gold Nanoparticle Enhancement of X-ray Scatter Imaging of Hepatocellular Carcinoma. Nano Letters. 2011; 11:2678–2683. [PubMed: 21644516]

Rosen JE, Chan L, Shieh D-B, Gu FX. Iron oxide nanoparticles for targeted cancer imaging and diagnostics. Nanomedicine: Nanotechnology, Biology and Medicine. 2012; 8:275–290.

Sistrom CL, Mckay NL. Costs, Charges, and Revenues for Hospital Diagnostic Imaging Procedures: Differences by Modality and Hospital Characteristics. Journal of the American College of Radiology. 2005; 2:511–519. [PubMed: 17411868]

Stampanoni M, Zhentian W, Thuring TD, Christian D, Roessl E, Trippel M, Kubik-Huch RA, Singer G, Hihl MK, Hauser N. The First Analysis and Clinical Evaluation of Native Breast Tissue Using Differential Phase-Contrast Mammography. Investigative Radiology. 2011; 46:801–806. [PubMed: 21788904]

Stein AF, Ilavsky J, Kopace R, Bennett EE, Wen H. Selective imaging of nano-particle contrast agents by a single shot x-ray diffraction technique. Optics Express. 2010; 18:13271–13278. [PubMed: 20588456]

Stephen ZR, Kievit FM, Zhang M. Magnetite nanoparticles for medical MR imaging. Materials Today. 2011; 14:330–338. [PubMed: 22389583]

Trevisani F, Cantarini MC, Wands JR, Bernardi M. Recent advances in the natural history of hepatocellular carcinoma. Carcinogenesis. 2008; 29:1299–1305. [PubMed: 18515282]

Vollrath A, Schubert S, Schubert US. Fluorescence imaging of cancer tissue based on metal-free polymeric nanoparticles - a review. Journal of Materials Chemistry B. 2013; 1:1994–2007.

Walkey CD, Olsen JB, Guo H, Emili A, Chan WCW. Nanoparticle Size and Surface Chemistry Determine Serum Protein Adsorption and Macrophage Uptake. J. Am. Chem. Soc. 2012; 134:2139–2147. [PubMed: 22191645]

Wen H, Bennett EE, Hegedus MM, Carroll SC. Spatial Harmonic Imaging of X-ray Scattering - Initial Results. IEEE Trans Med Imaging. 2008; 27:997–1002. [PubMed: 18672418]

Wen H, Bennett EE, Hegedus MM, Rapacchi S. Fourier X-ray Scattering Radiography Yields Bone Structural Information. Radiology. 2009; 251:910–918. [PubMed: 19403849]

Wu B, Liu Y, Rose-Petruck C, Diebold GJ. X-ray spatial frequency heterodyne imaging. Applied Physics Letters. 2012; 100:061110.

Yashiro W, Terui Y, Kawabata K, Momose A. On the origin of visibility contrast in x-ray Talbot interferometry. Optics Express. 2010; 18:16890–16901. [PubMed: 20721081]


**Figure 1.**
Schematic of the x-ray imaging setup.

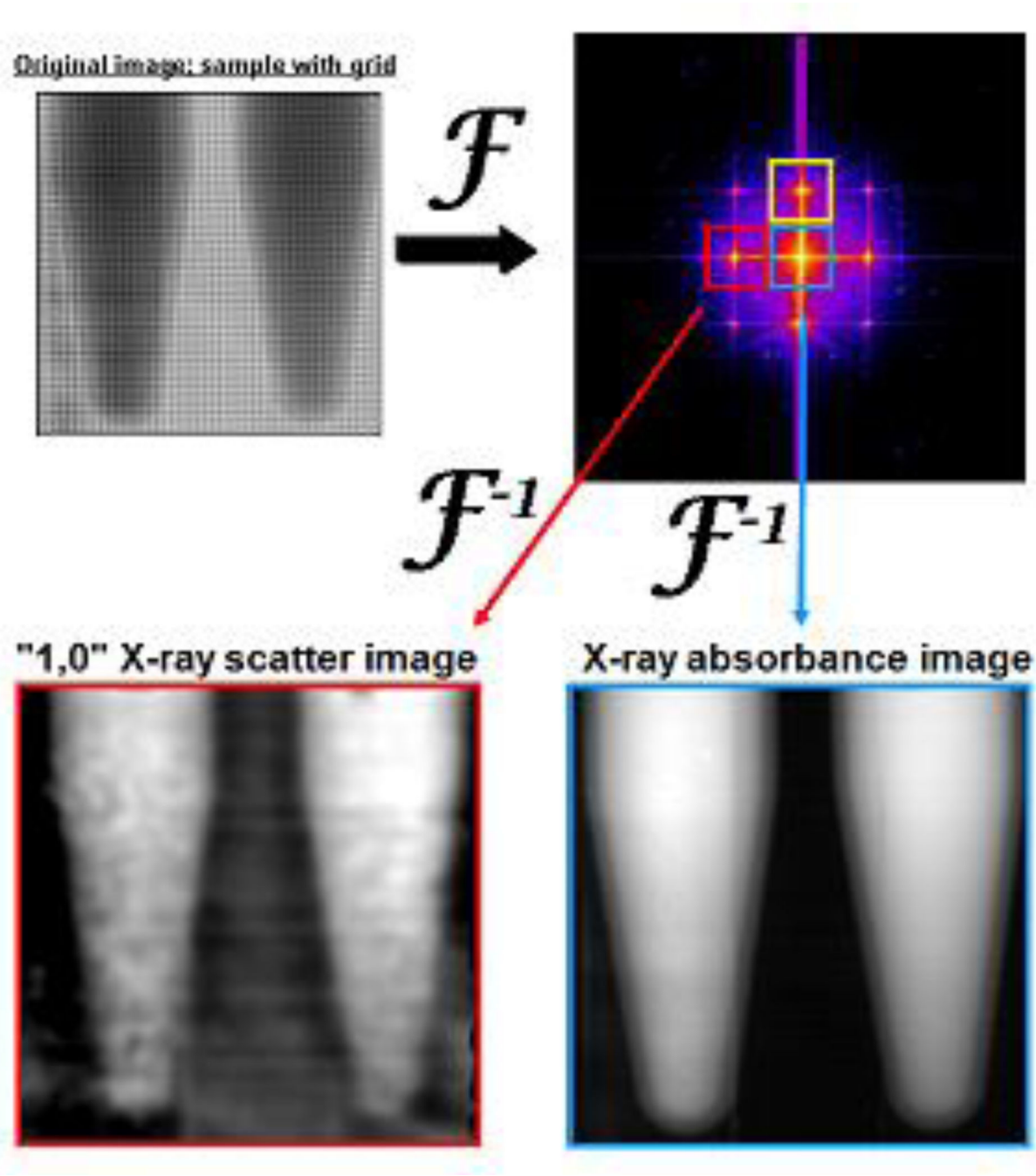


**Figure 2.**

Fourier transformation of an image with grid and sample placed in the x-ray beam path (top left) gives a convolution in the spatial frequency domain (top right). Different peaks in the spatial frequency spectrum (surrounded by colored boxes) contain different information regarding how the sample scatters and absorbs incident x-radiation.

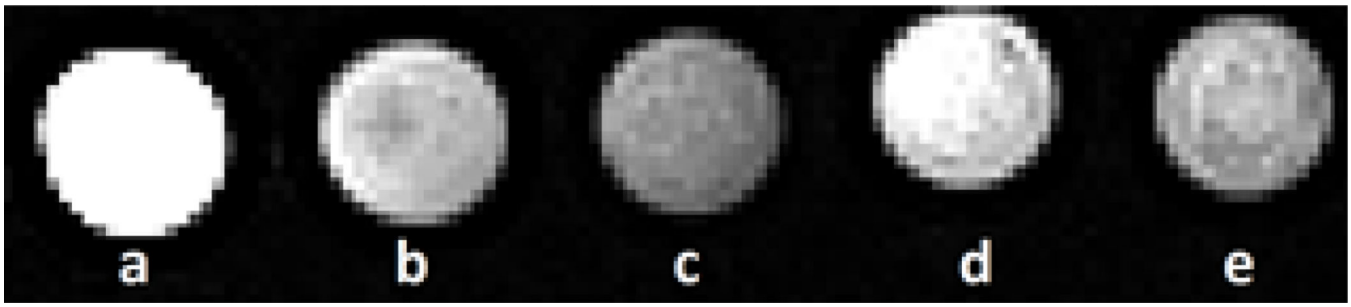


**Figure 3.**

MR images of HCC cells containing no iron (a), 10 nm SPION-COOH-PAH (b and c), and 40 nm SPION-COOH-PAH (d and e). The cells were incubated with iron oxide nanoparticles at 10 ppm iron concentration (b and d) or 20 ppm iron concentration (c and e).

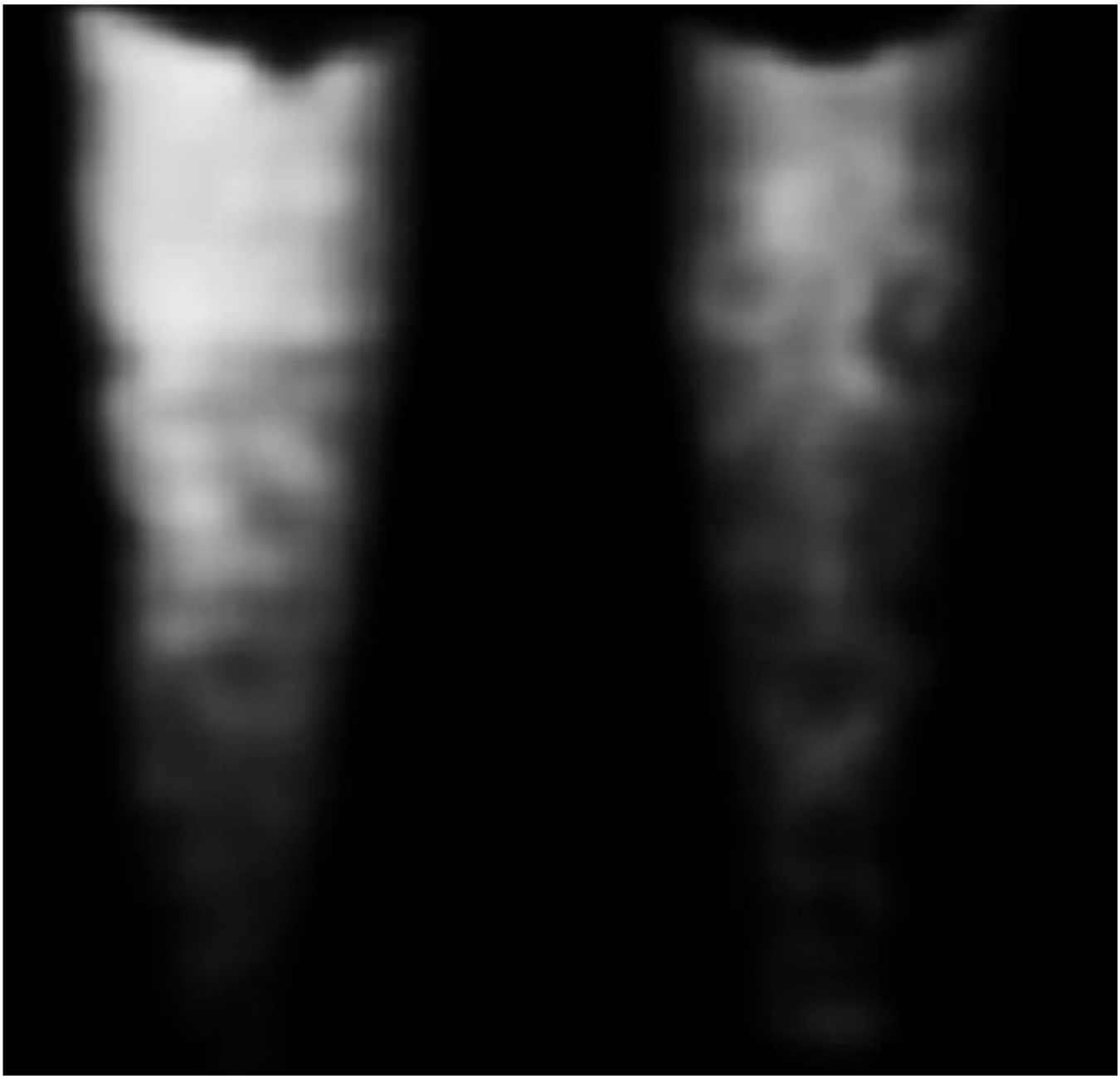

**Figure 4.**
SFHI x-ray scatter image of FOCUS cells incubated with 10 nm SPION-COOH-PAH at 20 ppm (left) and FOCUS cells without SPIONs (right).

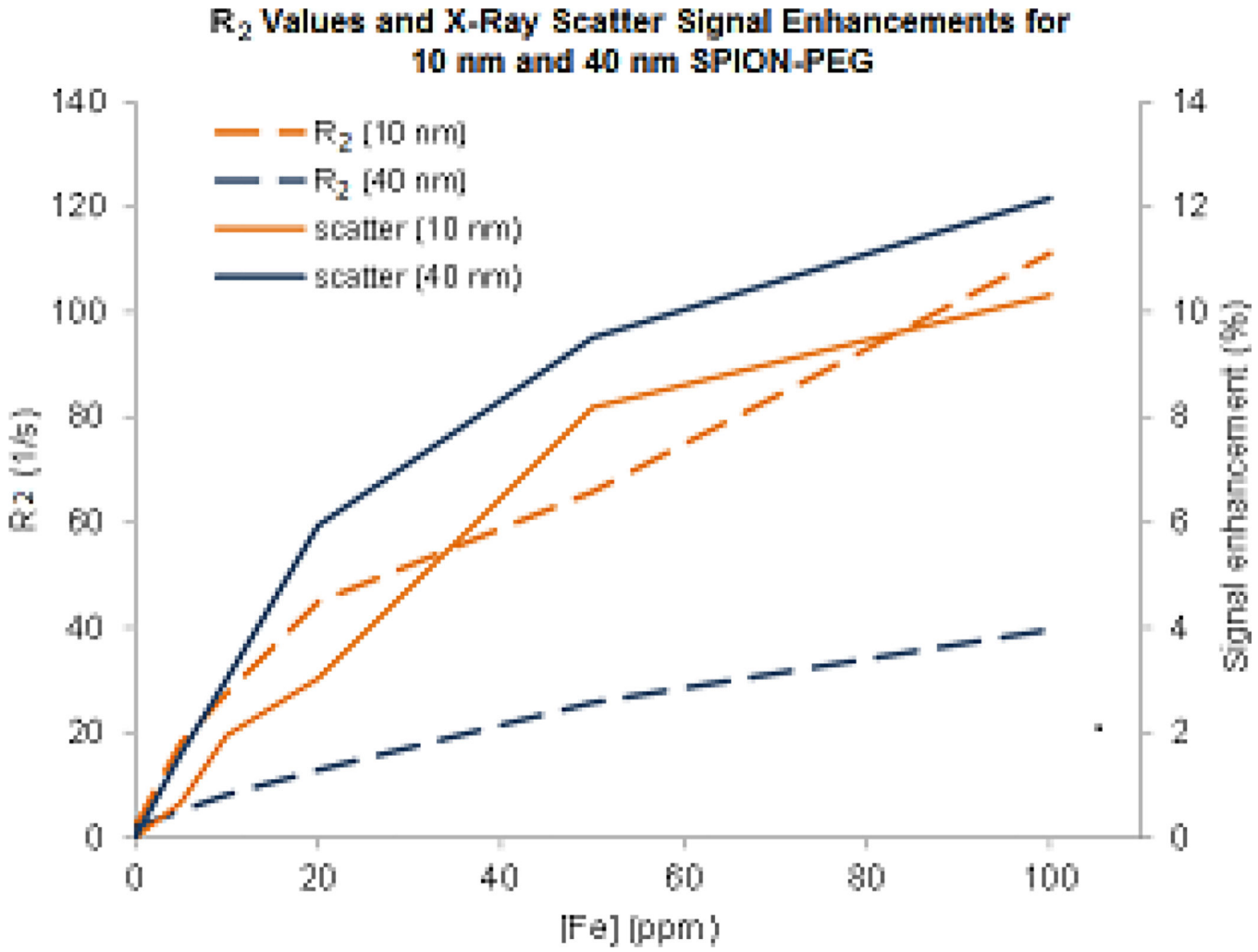


**Figure 5.**

Comparison of the change in relaxivity of 10 nm and 40 nm SPIONs in MRI (dashed lines, left y-axis) with the change in signal enhancement of 10 nm and 40 nm SPIONs in SFHI (dotted and solid lines, right y-axis).

## Table 1

Signal enhancements over water for 10 nm AuNP-PEG and 10 nm SPION-PEG as measured from SFHI x-ray scatter and x-ray absorbance images.

| [metal] (ppm) | x-ray absorbance signal enhancement (%) | | x-ray scatter signal enhancement (%) | |
|---|---|---|---|---|
| | 10 nm AuNP-PEG | 10 nm SPION-PEG | 10 nm AuNP-PEG | 10 nm SPION-PEG |
| 250 | 0.7 ± 0.03 | 0.5 ± 0.01 | 4.6 ± 0.23 | 6.1 ± <0.01 |
| 500 | 0.7 ± 0.01 | 0.6 ± 0.01 | 8.0 ± 0.47 | 7.6 ± 0.65 |
| 750 | 0.9 ± <0.01 | 0.6 ± <0.01 | 9.1 ± <0.01 | 7.9 ± 0.63 |
| 1000 | 1.0 ± 0.01 | 0.6 ± 0.01 | 12.0 ± 0.02 | 9.7 ± 0.24 |

## Table 2

$T_2$ relaxation times and x-ray scatter signal enhancements of 10 nm and 40 nm SPION-PEG.

| [Fe] (ppm) | $T_2$ relaxation time (ms) | | x-ray scatter signal enhancement (%) | |
|---|---|---|---|---|
| | 10 nm SPION-PEG | 40 nm SPION-PEG | 10 nm SPION-PEG | 40 nm SPION-PEG |
| 0 | 491 ± 61.3 | 491 ± 61.3 | N/A | N/A |
| 5 | 55 ± 2.1 | 196 ± 15.6 | 0.7 ± 0.75 | 1.6 ± 0.40 |
| 10 | 37 ± 3.4 | 123 ± 31.6 | 1.9 ± 0.08 | 3.0 ± 0.44 |
| 20 | 22 ± 4.3 | 78 ± 1.8 | 3.0 ± 0.50 | 5.9 ± 0.48 |
| 50 | 15 ± 8.2 | 39± 8.8 | 8.2 ± 0.28 | 9.5 ± 0.29 |
| 100 | <10 | 25 ± 6.3 | 10.3 ± 0.61 | 12.2 ± 0.10 |

## Table 3

Zeta potential and cellular uptake of 10 nm and 40 nm SPIONs before and after coating with poly(acrylic acid).

| | 10 nm | | 40 nm | |
|---|---|---|---|---|
| | **SPION-COOH** | **SPION-COOH-PAH** | **SPION-COOH** | **SPION-COOH-PAH** |
| zeta potential (mV) | −42 ± 3.1 | 54 ± 1.8 | −27.2 ± 1.5 | 38 ± 2.9 |
| mass of Fe taken up by $3 \times 10^6$ FOCUS cells (μg) | 2.0 ± 0.06 | 34.4 ± 3.97 | 8.4 ± 0.19 | 38.2 ± 1.47 |

**Table 4**

MRI and x-ray imaging of samples containing SPION-labeled HCC cells.

| | [Fe] during incubation (ppm) | mass of Fe taken up by $3 \times 10^6$ HCC cells (μg) | $T_2$ relaxation time (ms) | x-ray absorbance signal enhancement (%) | x-ray scatter signal enhancement (%) |
|---|---|---|---|---|---|
| FOCUS | 0 | 0 | 290 ± 30.5 | N/A | N/A |
| FOCUS + 10 nm SPION-COOH-PAH | 10 | 16.8 ± 0.53 | 150 ± 17.2 | 1.1 ± 0.01 | 18.3 ± 0.29 |
| | 20 | 40.5 ± 0.74 | 115 ± 11.8 | 1.2 ± 0.01 | 23.4 ± 0.69 |
| FOCUS + 40 nm SPION-COOH-PAH | 10 | 7.9 ± 0.19 | 223 ± 13.7 | 1.1 ± 0.01 | 16.1 ± 0.61 |
| | 20 | 17.9 ± 0.12 | 191 ± 11.4 | 1.2 ± 0.01 | 18.0 ± 0.45 |

**Table 5**

Comparison of three imaging techniques: traditional x-ray absorbance imaging, the novel SFHI, and MRI

| | Change in signal relative to HCC alone (%) | | | Relative Sensitivity | | Relative Uncertainty | Image Enhancement Factor |
|---|---|---|---|---|---|---|---|
| | X-ray Abs. | SFHI | MRI | SFHI / X-ray Abs. | MRI / SFHI | MRI / SFHI | MRI / SFHI |
| FOCUS + 10 ppm 10 nm SPION | 1.1 ± 0.01 | 18.3 ± 0.29 | 94.1 ± 4.27 | 16.3 | 5.2 | 2.9 | 1.8 |
| FOCUS + 20 ppm 10 nm SPION | 1.2 ± 0.01 | 23.4 ± 0.69 | 152.4 ± 5.24 | 20.0 | 6.5 | 1.2 | 5.6 |
| FOCUS + 10 ppm 40 nm SPION | 1.1 ± 0.01 | 16.1 ± 0.61 | 30.1 ± 2.17 | 14.2 | 1.9 | 1.9 | 1.0 |
| FOCUS + 20 ppm 40 nm SPION | 1.2 ± 0.01 | 18.0 ± 0.45 | 51.9 ± 2.50 | 15.5 | 2.9 | 1.9 | 1.5 |